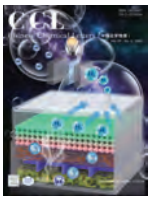
Chinese Chemical Letters 37 (2026) 111217

Contents lists available at ScienceDirect

Chinese Chemical Letters

journal homepage: www.elsevier.com/locate/cclet



Mechanism and origins of enantioselectivity of iridium-catalyzed atroposelective intermolecular C(sp^2)-H silylation: A ligand-enabled axial chirality transfer strategy

Deng Pan[a], Chuan He[b,*], Genping Huang[a,*]

[a] Department of Chemistry, School of Science, Tianjin University, Tianjin 300072, China
[b] Shenzhen Grubbs Institute and Department of Chemistry, Shenzhen Key Laboratory of Small Molecule Drug Discovery and Synthesis, Guangdong Provincial Key Laboratory of Catalysis, Southern University of Science and Technology, Shenzhen 518055, China

ARTICLE INFO

Article history:
Received 14 January 2025
Revised 6 April 2025
Accepted 15 April 2025
Available online 17 April 2025

Keywords:
C-H silylation
Iridium
DFT calculations
Reaction mechanism
enantioselectivity

ABSTRACT

Density functional theory calculations were performed to investigate the iridium-catalyzed atroposelective intermolecular C–H silylation of 2-arylisoquinolines. The Ir(III) hydride species was identified as the active catalyst species of the reaction. The computations show that the reaction occurs through the Ir(III)/Ir(V) catalytic cycle. The C(sp^2)-H oxidative addition represents the rate- and enantioselectivity-determining step. The distortion/interaction and structural analyses reveal that the BINEPINE skeleton of the PSiSi ligand creates an axially chiral pocket for the C–H oxidative addition, providing a ligand-enabled axial chirality transfer strategy responsible for the observed enantioselectivity. The match/mismatch in axial chirality between reacting 2-arylisoquinolines and the BINEPINE skeleton of the PSiSi ligand plays a key role in governing enantioselectivity.

© 2026 Published by Elsevier B.V. on behalf of Chinese Chemical Society and Institute of Materia Medica, Chinese Academy of Medical Sciences.

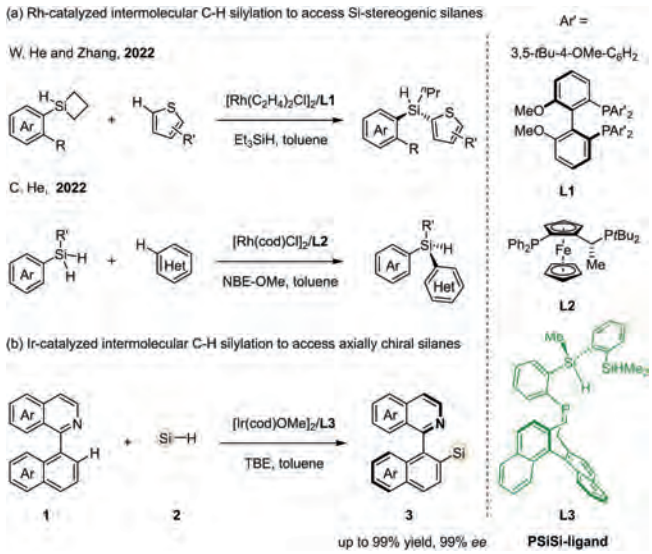
Chiral silicon-containing organic compounds have attracted significant interest due to their unique properties in chemistry, physics, biology, and stereoelectronics, enabling diverse applications in materials science, pharmaceuticals, and agricultural sciences [1–3]. Therefore, the development of efficient methodologies for the synthesis of these compounds is of paramount significance in organic synthesis [4–7]. In this context, transition metal-catalyzed enantioselective C–H silylation reactions have emerged as one of the most atom-economical and straightforward approaches, attracting substantial research interest over the years [8–16]. Nonetheless, while considerable research has been devoted to the intramolecular C–H silylation reactions [17–24], the intermolecular C–H silylation reactions [25–28], particularly in terms of variations in stereoselectivity, remains a relatively unexplored area and presents a significant challenge in this field (Scheme 1). In this context, He, Zhang, and co-workers in 2022 reported the rhodium-catalyzed enantioselective intermolecular C–H silylation of thiophenes with silacyclobutanes (Scheme 1a, up) [25]. In parallel, He and co-workers realized a first example of the rhodium-catalyzed enantioselective intermolecular dehydrogenative C–H silylation of thiophenes and furans (Scheme 1a, below) [26]. Later, Chen, Huang, and co-workers also established a similar strategy for the enantioselective synthesis of acyclic monohydrosilanes *via* rhodium-catalyzed intermolecular dehydrogenative C–H silylation with heterocyclic compounds [27].

Although rapid progress has been made, these studies have been limited to the asymmetric synthesis of acyclic, silicon-stereogenic silanes (Scheme 1a). Very recently, C. He and co-workers developed the first iridium-catalyzed atroposelective intermolecular C–H silylation of 2-arylisoquinolines, offering a powerful protocol for accessing a series of axially chiral silanes with exceptional yields and enantioselectivities (Scheme 1b) [28]. The key to the success of this transformation lies in the use of the novel chiral PSiSi-ligand. It was found that with a combination of $[Ir(OMe)(cod)]_2$ and chiral PSiSi ligand **L3**, using the 3,3-dimethylbut-1-ene (TBE) as a hydrogen acceptor, the 2-arylisoquinolines **1** undergo atroposelective C–H silylation with hydrosilanes **2** to afford products **3** in high yields (up to 99%) and excellent enantioselectivities (up to 99% *ee*). To gain a better understanding of the reaction mechanism, parallel kinetic isotope effect (KIE) experiments were conducted, showing that the Si-H bond cleavage does not occur in the rate-determining step, whereas C–H bond activation is involved in this critical step.

Despite the significant advancement in enantioselective C–H silylation, the mechanistic studies in this area remain scarce and are primarily focused on the intramolecular reactions [29–31]. For

* Corresponding authors.
E-mail addresses: hec@sustech.edu.cn (C. He), gphuang@tju.edu.cn (G. Huang).

https://doi.org/10.1016/j.cclet.2025.111217
1001-8417/© 2026 Published by Elsevier B.V. on behalf of Chinese Chemical Society and Institute of Materia Medica, Chinese Academy of Medical Sciences.



Scheme 1. Rh- and Ir-catalyzed enantioselective intermolecular C(sp^2)-H silylation.

instance, we previously reported a computational investigation of iridium-catalyzed intramolecular silylation of unactivated C(sp^3)–H bonds, wherein the *in situ* generated iridium(III) silyl dihydride species was found to be the active catalyst [29]. More recently, He and co-workers conducted a combined experimental and computational study on the rhodium-catalyzed intramolecular enantioselective C–H silylation with dihydrosilanes [30]. Following our continuous interest in this field, we therefore decided to investigate the title reaction by means of density functional theory (DFT) calculations [32–42]. Interestingly, the computations unveil a ligand-enabled axial chirality transfer strategy responsible for the observed enantioselectivity, arising from the match/mismatch in axial chirality between the reacting 2-arylisoquinolines and the BINEPINE skeleton of the PSiSi ligand.

All the calculations were performed using Gaussian 09 package [43]. The geometry optimizations were carried out at the B3LYP-D3(BJ) [44–46]. Level of theory with a mixed basis set of SDD for Ir and 6–31G(d) for all other atoms. Frequencies were computed analytically at the same level of theory to confirm whether the structures are minima (no imaginary frequencies) or transition states (only one imaginary frequency). Selected transition-state structures were confirmed to connect the correct reactants and products by intrinsic reaction coordinate (IRC) calculations [47,48]. To obtain better accuracy, energies for the optimized geometries were re-calculated with M06 functional [49,50]. using the solution-phase single-point calculations with a larger basis set, which is SDD for Ir and 6–311+G(d,p) for all other atoms. Solvation effects (solvent = toluene, ε=2.3741) were taken into account by performing single-point calculations with the SMD model [51]. The final free energies reported in the article are the large basis set single-point energies corrected by gas-phase Gibbs free energy correction (at 298.15 K). All 3D structures of the optimized geometries were generated using CYLview [52].

The experimentally used 1-(naphthalen-1-yl)isoquinoline **1a** and dimethyl(phenyl)silane **2a** were selected as the model substrates in the calculations. Experimentally, the stoichiometric reactions suggest that the Ir(III) catalyst complex **IM1**, generated *in situ* by the reaction of Ir(I) precursor [Ir(cod)OMe]$_2$ with chiral PSiSi-ligand **L3** *via* a dehydrogenative process, is the plausible catalyst species of the reaction [6]. Therefore, the Ir(III) catalyst complex **IM1** was used as the starting point of the calculations. The sum of the free energies of **IM1** and substrates were chosen to be the zero on the relative free energy scale (Fig. 1).

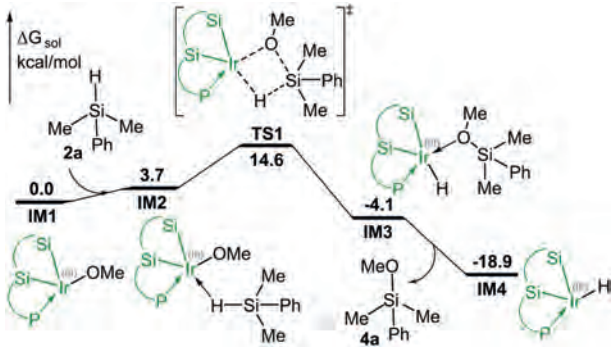


Fig. 1. Calculated energy profile for the formation of active catalyst species **IM4**.

At the outset, the formation of the iridium(III) hydride intermediate **IM4** was considered (Fig. 1). The process begins with the coordination of **2a** to the Ir(III) center of **IM1** to form intermediate **IM2**, which was calculated to be endergonic by 3.7 kcal/mol. Then, the σ-bond metathesis was found to occur *via* transition state **TS1** with an energy barrier of 14.6 kcal/mol relative to **IM1**, giving rise to intermediate **IM3** The subsequent dissociation of methoxydimethyl(phenyl)silane **4a** from the Ir(III) center leads to iridium(III) hydride intermediate **IM4**. The computations show that the formation of intermediate **IM4** is highly exergonic by 18.9 kcal/mol. Notably, the intermediate **IM4** is identified as the active catalyst species of the reaction (*vide infra*). It is also worth mentioning that the iridium(III) hydride intermediate has previously been proposed as the active catalytic species in the related Ir-catalyzed intramolecular C–H silylation reactions [7].

The calculated energy profile of the most favorable pathway for the intermolecular C–H silylation catalyzed by active catalyst species **IM4** is depicted in Fig. 2. Other possible reaction pathways starting from intermediate **IM4** were deposited in Fig. S2 (Supporting information). Starting from **IM4**, the coordination of the C=C double bond of TBE to the Ir(III) center delivers π-complex **IM5**, which was calculated to be exergonic by 9.4 kcal/mol. Then, **IM5** undergoes the 2,1-migratory insertion of C=C double bond into the Ir–H bond *via* transition state **TS2**, with an energy barrier of 10.6 kcal/mol relative to **IM5**. The alternative 1,2-migratory insertion was also considered, but it was found to be significantly higher in energy compared to the 2,1-migratory insertion (Fig. S1 in Supporting information for details). The resulting intermediate **IM6** is much less stable than **IM5** by 9.5 kcal/mol. With the incoming **2a**, the ensuing Si-H oxidative addition takes place through transition state **TS3** to furnish iridium(V) silyl hydride species **IM7**, requiring an energy barrier of 11.4 kcal/mol relative to **IM6** (*i.e.*, 20.9 kcal/mol relative to **IM5**). The iridium(V) silyl hydride species **IM7** was found to be relatively unstable, and can readily undergo the C–H reductive elimination *via* transition state **TS4** to form iridium(III) silyl species **IM8** and release 2,2-dimethylbutane, with an energy barrier of only 3.7 kcal/mol relative to **IM7**. The computations show that formation of iridium(III) silyl species **IM8** from iridium(III) hydride intermediate **IM4** is thermodynamically favored by as much as 24.9 kcal/mol. This substantial energy difference provides the driving force for the overall reaction, underscoring the critical role of TBE in promoting this transformation.

Upon formation of iridium(III) silyl species **IM8**, the next step of the reaction is the C–H oxidative addition, other possible C–H oxidative addition starting from intermediate **IM8** (see Fig. S4 in Supporting information for details). The coordination of the incoming **1a** to the Ir(III) center gives intermediate **IM9**. The subsequent C–H oxidative addition occurs *via* transition state **TS5**, giving rise to iridium(V) intermediate **IM10**. The computations show that this step is endergonic by 19.0 kcal/mol. Finally, the catalytic cycle is

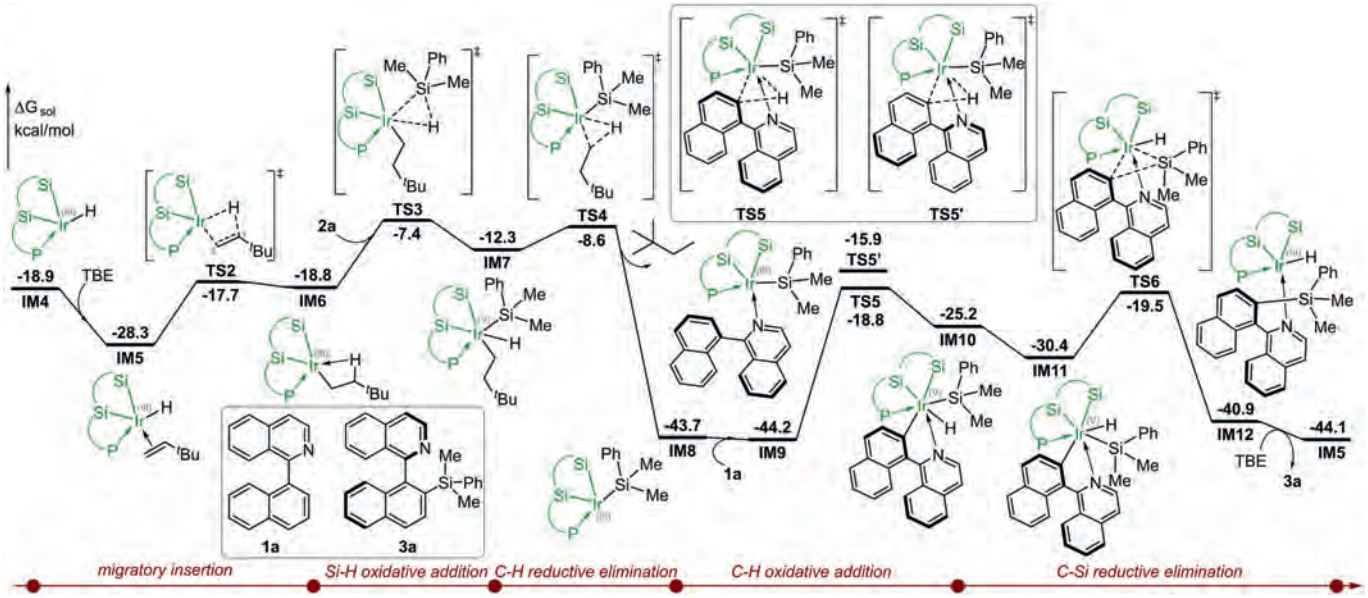


Fig. 2. Calculated energy profile of Ir-catalyzed atroposelective intermolecular C-H silylation of **1a**.

completed by the C−Si reductive elimination to form the C(sp^2)−H silylation product **3a**. However, the C-Si reductive elimination cannot take place directly from **IM10**, since the H ligand occupies the coordination site between the aryl group and the silyl ligand. Therefore, an isomerization step for the positional change of the hydride ligand is required prior to the C-Si reductive elimination. The computations show that isomerization process is kinetically feasible (Fig. S3 in Supporting information for details). The resulting intermediate **IM11**, in which the aryl group is adjacent to the silyl ligand, was found to be more stable than **IM10** by 5.2 kcal/mol. Then, **IM11** can undergo the C-Si reductive elimination *via* transition state **TS6** to afford product-coordinated intermediate **IM12**, from which the ligand exchange with TBE results in the formation of product **3a** and Ir(III) complex **IM5**.

The computations reveal that the C–H oxidative addition constitutes the rate- and enantioselectivity-determining step of the overall reaction, which is in accordance with the KIE experiments. The computed energy difference of 2.9 kcal/mol between **TS5** and **TS5′** (−18.8 *versus* −15.9 kcal/mol) corresponds to a predicted ratio of 99:1 at the reaction temperature, which aligns well with the experimentally observed excellent enantioselectivity. The optimized geometries of transition states **TS5** and **TS5′** are displayed in Fig. 3a. It was found that the key bond distances in two transition states are very different. In particular, the breaking C–H bond in **TS5** is greater than that in **TS5′** by 0.25 Å (1.72 *versus* 1.47 Å), implying that transition state **TS5** is significantly later than **TS5′**.

To further elucidate the origins of the enantioselectivity, the distortion/interaction analysis along the reaction pathway was conducted, using the breaking C–H bond distances as a reaction coordinate (Fig. 3b) [53]. The results show that the interaction energies of **TS5′**are constantly greater than that of **TS5** along the reaction pathway, while the distortion energies of **TS5′** are higher than that of **TS5**, being the dominant factor that contributes to the enantioselectivity. Further analysis reveals that the difference in distortion energies primarily arises from 1-(naphthalen-1-yl)isoquinoline **1a** moiety (Fig. S5 in Supporting information for details). Thus, the geometric changes of **1a** along the reaction pathway play a critical role in determining enantioselectivity. The structural analysis of **IM8** moiety shows that the silyl group and the PSiSi ligand on the Ir atom create a compact environment for incoming **1a** (Fig. 3c). Importantly, an axially chiral pocket was generated by

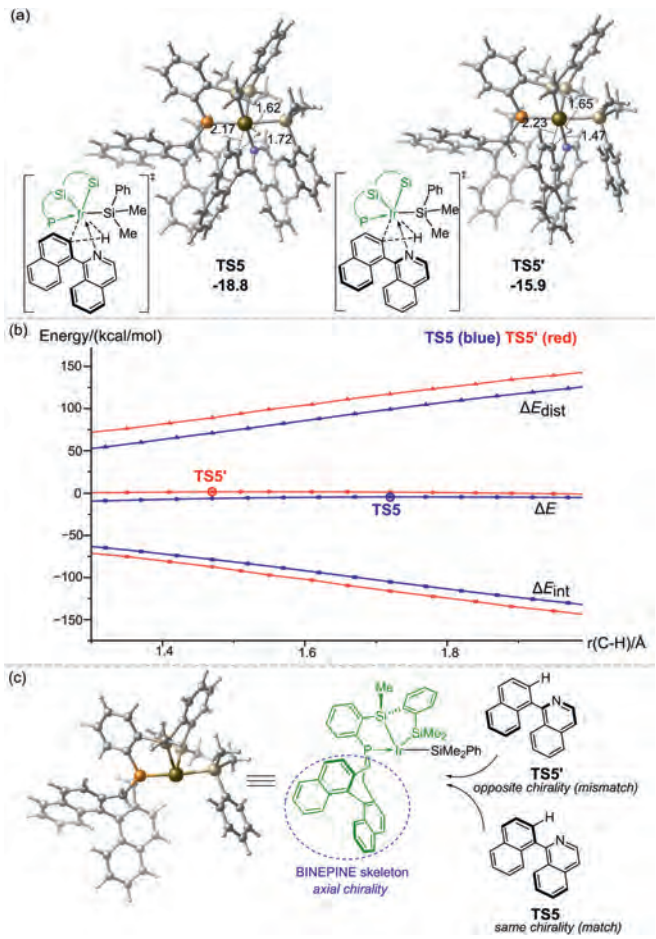


Fig. 3. (a) Optimized geometries of transition states **TS5** and **TS5′**. (b) Distortion/interaction analysis along the reaction pathway. (c) Structural analysis of **IM8** moiety. The energies and bond distances are given in kcal/mol and Å, respectively.

the BINEPINE skeleton of the PSiSi ligand. In **TS5**, **1a** adopts the same axial chirality as the BINEPINE skeleton, requiring minimal geometric adjustment. By contrast, in **TS5′**, the axial chirality of **1a** is opposite to that of the BINEPINE skeleton, necessitating a larger geometric change to reach the transition state structure. Consequently, the axial chirality of the PSiSi ligand is directly transferred to the reaction, dictated by the match/mismatch in axial chirality between **1a** and the BINEPINE skeleton of the PSiSi ligand.

To summarize, we have presented a mechanistic study on the iridium(III)-catalyzed intermolecular C–H silylation of 2-arylisoquinolines by means of DFT calculations. The computations show that the iridium(III) hydride species is the active catalyst of the reaction. The reaction was found to proceed through the Ir(III)/Ir(V) catalytic cycle, consisting of five major steps: (1) Migratory insertion of TBE into the Ir–H bond, (2) Si-H oxidative addition to form iridium(V) silyl hydride species, (3) C–H reductive elimination to generate the iridium(III) silyl species, (4) C(sp^2)-H oxidative addition to yield the iridium(V) complex, and (5) C-Si reductive elimination to deliver the final silylation product. The C(sp^2)-H oxidative addition constitutes the rate- and enantioselectivity-determining step of the overall reaction. The distortion/interaction and structural analyses reveal a ligand-enabled axial chirality transfer strategy responsible for the observed enantioselectivity. Specifically, the BINEPINE skeleton of the PSiSi ligand creates an axially chiral pocket for the C–H oxidative addition. The match/mismatch in axial chirality between reacting 2-arylisoquinolines and the BINEPINE skeleton of the PSiSi ligand plays a pivotal role in controlling enantioselectivity. The computations should provide important implications for a better understanding of the related C–H silylation reactions and the development of new catalytic systems.

Declaration of competing interest

The authors declare that they have no known competing financial interests or personal relationships that could have appeared to influence the work reported in this paper.

CRediT authorship contribution statement

Deng Pan: Writing – review & editing, Writing – original draft, Investigation. **Chuan He:** Writing – review & editing, Conceptualization. **Genping Huang:** Writing – review & editing, Writing – original draft, Funding acquisition, Conceptualization.

Acknowledgments

This work was supported by the National Natural Science Foundation of China (Nos. 22471191, 22073066, and 22271134), and Shenzhen Science and Technology Innovation Commission (Nos. RCJC20221008092723013, JCYJ20230807093104009).

Supplementary materials

Supplementary material associated with this article can be found, in the online version, at doi:10.1016/j.cclet.2025.111217.

References

[1] A.K. Franz, S.O. Wilson, J. Med. Chem. 56 (2013) 388–405.
[2] B.A. Kamino, T.P. Bender, Chem. Soc. Rev. 42 (2013) 5119–5130.
[3] Y. Zuo, Z. Gou, W. Quan, W. Lin, Coord. Chem. Rev. 438 (2021) 213887.
[4] E. Langkopf, D. Schinzer, Chem. Rev. 95 (1995) 1375–1408.
[5] L.W. Xu, L. Li, G.Q. Lai, J.X. Jiang, Chem. Soc. Rev. 40 (2011) 1777–1790.
[6] C.G. Newton, S.G. Wang, C.C. Oliveira, N. Cramer, Chem. Rev. 117 (2017) 8908–8976.
[7] Y. Wu, P. Wang, Angew. Chem. Int. Ed. 61 (2022) e202205382.
[8] J.F. Hartwig, Acc. Chem. Res. 45 (2012) 864–873.
[9] C. Cheng, J.F. Hartwig, Chem. Rev. 115 (2015) 8946–8975.
[10] Z. Xu, L.W. Xu, ChemSusChem 8 (2015) 2176–2179.
[11] S.C. Richter, M. Oestreich, Trends Chem. 2 (2020) 13–27.
[12] B. Li, P.H. Dixneuf, Chem. Soc. Rev. 50 (2021) 5062–5085.
[13] Y. Ge, X. Huang, J. Ke, C. He, Chem Catal. 2 (2022) 2898–2928.
[14] C.X. Liu, S.Y. Yin, F. Zhao, et al., Chem. Rev. 123 (2023) 10079–10134.
[15] Y. Wu, L. Zheng, Y. Wang, P. Wang, Chem 9 (2023) 3461–3514.
[16] H. Khatua, S. Das, S. Patra, B. Chattopadhyay, Synthesis 55 (2023) 3434–3453.
[17] L.W. Xu, Angew. Chem. Int. Ed. 51 (2012) 12932–12934.
[18] Q.W. Zhang, K. An, L.C. Liu, et al., Angew. Chem. Int. Ed. 56 (2017) 1125–1129.
[19] D. Mu, W. Yuan, S. Chen, et al., J. Am. Chem. Soc. 142 (2020) 13459–13468.
[20] B. Yang, W. Yang, Y. Guo, L. You, C. He, Angew. Chem. Int. Ed. 59 (2020) 22217–22222.
[21] W. Ma, L.C. Liu, K. An, T. He, W. He, Angew. Chem. Int. Ed. 60 (2021) 4245–4251.
[22] S. Chen, D. Mu, P. Mai, et al., Nat. Commun. 12 (2021) 1249.
[23] Y. Guo, M.M. Liu, X. Zhu, L. Zhu, C. He, Angew. Chem. Int. Ed. 60 (2021) 13887-1389.
[24] Y. Zeng, X.J. Fang, R.H. Tang, et al., Angew. Chem. Int. Ed. 61 (2022) e202214147.
[25] S. Chen, J. Zhu, J. Ke, Y. Li, C. He, Angew. Chem. Int. Ed. 61 (2022) e202117820.
[26] K. An, W. Ma, L.C. Liu, et al., Nat. Commun. 13 (2022) 847.
[27] D. Mu, S. Pan, X. Wang, et al., Chem. Commun. 58 (2022) 7388–7391.
[28] B. Yang, J. Gao, X. Tan, Y. Ge, C. He, Angew. Chem. Int. Ed. 62 (2023) e202307812.
[29] M. Zhang, J. Liang, G. Huang, J. Org. Chem. 84 (2019) 2372–2376.
[30] N. Li, J. Ke, L.Q. Ren, Y. Li, C. He, Chem Catal. 3 (2023) 100799.
[31] C. Karmel, J.F. Hartwig, J. Am. Chem. Soc. 142 (2020) 10494–10505.
[32] H. Tamura, H. Yamazaki, H. Sato, S. Sakaki, J. Am. Chem. Soc. 125 (2003) 16114–16126.
[33] A.G. Green, P. Liu, C.A. Merlic, K.N. Houk, J. Am. Chem. Soc. 136 (2014) 4575–4583.
[34] G. Huang, M. Kalek, R.Z. Liao, F. Himo, Chem. Sci. 6 (2015) 1735–1746.
[35] J. Jover, F. Maseras, Organometallics 35 (2016) 3221–3226.
[36] A. Unnikrishnan, R.B. Sunoj, Chem. Sci. 10 (2019) 3826–3835.
[37] B.E. Haines, Y. Saito, Y. Segawa, K. Itami, D.G. Musaev, ACS Catal. 6 (2016) 7536–7546.
[38] L. Zhu, X. Qi, Y. Li, et al., Organometallics 36 (2017) 2107–2115.
[39] R.L. Zhong, S. Sakaki, J. Am. Chem. Soc. 141 (2019) 9854–9866.
[40] R.L. Zhong, S. Sakaki, J. Am. Chem. Soc. 142 (2020) 16732–16747.
[41] M. Zhang, H. Wu, Yang J, G. Huang, ACS Catal. 11 (2021) 4833–4847.
[42] L.Y. Bao, J.S. Wang, L. Li, R.L. Zhong. Z.M. Su, J. Org. Chem. 89 (2024) 18047–18059.
[43] M.J. Frisch, G.W. Trucks, H.B. Schlegel, et al., Gaussian 09, Gaussian, Inc., Wallingford, CT, 2013.
[44] C. Lee, W. Yang, R.G. Parr, Phys. Rev. B. 37 (1988) 785–789.
[45] A.D. Becke, J. Chem. Phys. 98 (1993) 5648–5652.
[46] S. Grimme, J. Antony, S. Ehrlich, H. Krieg, J. Chem. Phys. 132 (2010) 154104.
[47] K. Fukui, J. Phys. Chem. 74 (1970) 4161–4163.
[48] K. Fukui, Acc. Chem. Res. 14 (1981) 363–368.
[49] Y. Zhao, D.G. Truhlar, Acc. Chem. Res. 41 (2008) 157–167.
[50] Y. Zhao, D.G. Truhlar, Theor. Chem. Acc. 120 (2008) 215–241.
[51] A.V. Marenich, C.J. Cramer, D.G. Truhlar, J. Phys. Chem. B 113 (2009) 6378–6396.
[52] C.Y. Legault, CYLview, ver. 1.0b, Université de Sherbrooke, 2009 http://www.cylview.org.
[53] F.M. Bickelhaupt, K.N. Houk, Angew. Chem. Int. Ed. 56 (2017) 10070–10086.